Supporting Information

Stark effect spectroscopy of mono- and few-layer MoS_2

AUTHOR NAMES.

J. Klein[1], J. Wierzbowski[1*], A. Regler[1,2], J. Becker[1], F. Heimbach[3], K. Müller[1,4], M. Kaniber[1†] and J. J. Finley[1†]*

AUTHOR ADDRESS.

[1] Walter Schottky Institut und Physik Department, Technische Universität München, Am Coulombwall 4, 85748 Garching, Germany

[2] Institute for Advanced Study, Technische Universität München, Lichtenbergstrasse 2a, 85748 Garching, Germany

[3] Lehrstuhl für Physik funktionaler Schichtsysteme, Physik Department E10, Technische Universität München, James-Franck-Straße 1, 85747 Garching, Germany

[4] E. L. Ginzton Laboratory, Stanford University, Stanford, CA 94305, USA

[†]Correspondence to kaniber@wsi.tum.de or finley@wsi.tum.de

[*] These authors contributed equally

Content

S1 Layer number identification

To identify the number of MoS_2 layers embedded in the photocapacitor devices, we utilised Raman spectroscopy. As reported in literature,[1] the in-plane E^1_{2g} and out-of-plane A_{1g} Raman modes are a clear fingerprint on the layer number.

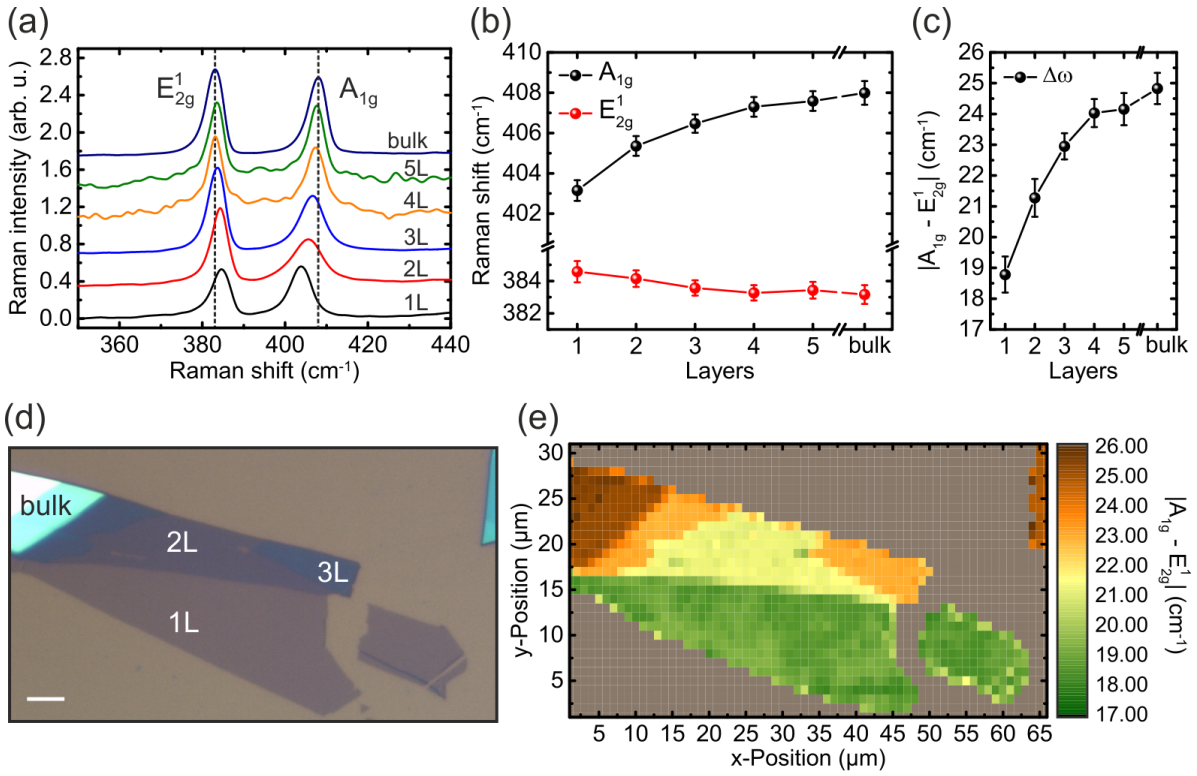

SI Figure 1. (a) Layer-dependent Raman spectra. The dashed lines mark the position of the E_{2g}^1 and A_{1g} modes for bulk material. All spectra are displaced for clarity. (b) Layer dependence of phonon modes plotted as a function of the layer number. (c) Difference of A_{1g} mode and E_{2g}^1 mode from (b) is plotted as a function of the layer number. (d) Optical microscope image of few-layer MoS_2. The scale bar is 5 µm. (e) Raman mapping of the mode difference $A_{1g} - E_{2g}^1$ clearly reveals the different layer numbers.

SI figure 1(a) shows Raman spectra of the in-plane and out-of-plane mode for different layer numbers and bulk material. Dashed lines define the position of the in-plane E_{2g}^1 and out-of-plane A_{1g} modes for bulk material. We can clearly identify an upshift of the A_{1g} and a downshift of the E_{2g}^1 mode for a higher number of layers. SI Figure 1(b) shows the corresponding position of both phonon modes depending on the number of layers. We obtain a shift from 403.2 cm^{-1} to 408 cm^{-1} for the A_{1g} mode and a shift from 384.6 cm^{-1} to 383.1 cm^{-1} for the E_{2g}^1 mode from monolayer to bulk material. By plotting the difference between both modes as presented in SI figure 1(c) we observe an overall increase from 18.6 cm^{-1} to 24.9 cm^{-1} from a single layer to bulk material. We can utilise $A_{1g} - E_{2g}^1$ as a clear fingerprint to identify the layer number. SI figure 1(d) depicts an optical microscope image of exfoliated few-layer MoS_2 on a Si wafer covered with 290 nm SiO_2. SI figure 1(e) shows the corresponding Raman mapping of SI figure 1(d) where the mode difference is plotted as a function of the spatial position. The differently coloured areas can be immediately assigned to monolayer, bilayer, trilayer and bulk material. For additional validation, we applied the transfer matrix method[2] to calculate the phase contrast up to many layers.

S2 Calculation of the device capacitance

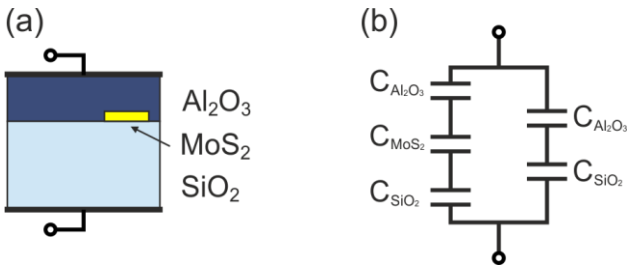

SI Figure 2. (a) Theoretical device structure. Two stacking areas of $Al_2O_3/MoS_2/SiO_2$ and Al_2O_3/SiO_2 sandwiched between two metallic plates. (b) Corresponding circuit diagram of the capacitor.

For our theoretical considerations we take into account a stacking of Al_2O_3, MoS_2 and SiO_2 sandwiched between two metallic plates as depicted in SI figure 2(a). The presence of MoS_2 separates the complete area of the top-gate into an area A_{w,MoS_2} with MoS_2 and an area A_{wo,MoS_2} without. The full circuit diagram for this configuration is shown in SI figure 2(b). The total capacitance of the system is a parallel circuit of these two different areas given as follows

$$C_{tot} = C_{w,MoS_2} + C_{wo,MoS_2} \quad (1)$$

with the capacitance C_{w,MoS_2} of the capacitor filled with MoS_2 and the capacitance C_{wo,MoS_2} without. Both values are given by a series connection of the different single capacitances of the respective layers, and are defined as follows

$$C_{w,MoS_2} = \left(\frac{1}{C^w_{Al_2O_3}} + \frac{1}{C^w_{MoS_2}} + \frac{1}{C^w_{SiO_2}} \right)^{-1} \quad (2)$$

$$C_{wo,MoS_2} = \left(\frac{1}{C^w_{Al_2O_3}} + \frac{1}{C^w_{SiO_2}}\right)^{-1}. (3)$$

With the formula $C = \varepsilon_0 \varepsilon_r \frac{A}{d}$ for a simple parallel plate capacitor, we can derive the total capacitance

$$C_{tot} = \varepsilon_0 \cdot \left[A_{w,MoS_2}\left(\frac{\varepsilon_{Al_2O_3}\varepsilon_{SiO_2}\varepsilon_{MoS_2}}{\varepsilon_{SiO_2}\varepsilon_{MoS_2}d_{Al_2O_3}+\varepsilon_{Al_2O_3}\varepsilon_{MoS_2}d_{SiO_2}+\varepsilon_{SiO_2}\varepsilon_{Al_2O_3}d_{MoS_2}}\right) + A_{wo,MoS_2}\left(\frac{\varepsilon_{Al_2O_3}\varepsilon_{SiO_2}}{\varepsilon_{SiO_2}d_{Al_2O_3}+\varepsilon_{Al_2O_3}d_{SiO_2}}\right)\right]. (4)$$

With the dielectric permittivities ($\varepsilon_{Al_2O_3} = 9.3$, $\varepsilon_{MoS_2} = 2.8$, $\varepsilon_{SiO_2} = 3.9$)[3] the layer thicknesses ($d_{Al_2O_3} = 20\ nm$, $d_{MoS_2} = 0.65\ nm$, $d_{SiO_2} = 200\ nm\ /\ 290\ nm$) and the corresponding gate area for the materials. By substituting the area without MoS_2 by making use of the relation $A_{wo,MoS_2} = A_{tot} - A_{w,MoS_2}$ we obtain the total capacitance as a function of the flake area as given by

$$C_{tot}(A_{w,MoS_2}) = \varepsilon_0 \cdot \left[A_{w,MoS_2}\left(\frac{\varepsilon_{Al_2O_3}\varepsilon_{SiO_2}\varepsilon_{MoS_2}}{\varepsilon_{SiO_2}\varepsilon_{MoS_2}d_{Al_2O_3}+\varepsilon_{Al_2O_3}\varepsilon_{MoS_2}d_{SiO_2}+\varepsilon_{SiO_2}\varepsilon_{Al_2O_3}d_{MoS_2}}\right) + (A_{tot} - A_{w,MoS_2})\left(\frac{\varepsilon_{Al_2O_3}\varepsilon_{SiO_2}}{\varepsilon_{SiO_2}d_{Al_2O_3}+\varepsilon_{Al_2O_3}d_{SiO_2}}\right)\right]. (5)$$

The total capacitance as a function of the crystal coverage in percent of the top-gate area for mono-, bi- and trilayer MoS_2 is plotted in SI figure 3 for 200 nm SiO_2 covered Si. The total capacitance is approximately independent on the MoS_2 coverage and layer number for the micro-crystallites used in our experiments. Based on our model, we can estimate a theoretical capacitance of $C_{theo} \sim (7.95 \pm 0.39)$ pF. The

error originates from uncertainties in the effective top-gate area and from uncertainties of the SiO_2 and Al_2O_3 thicknesses.

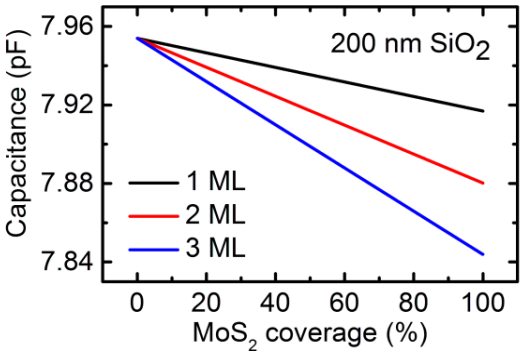

SI Figure 3. Calculated micro-capacitor capacitance from eq. 5 as a function of the MoS_2 crystal coverage for mono-, bi- and trilayer material on p-doped Si substrate with 200 nm SiO_2.

S3 Device transfer characteristics and electric field simulations

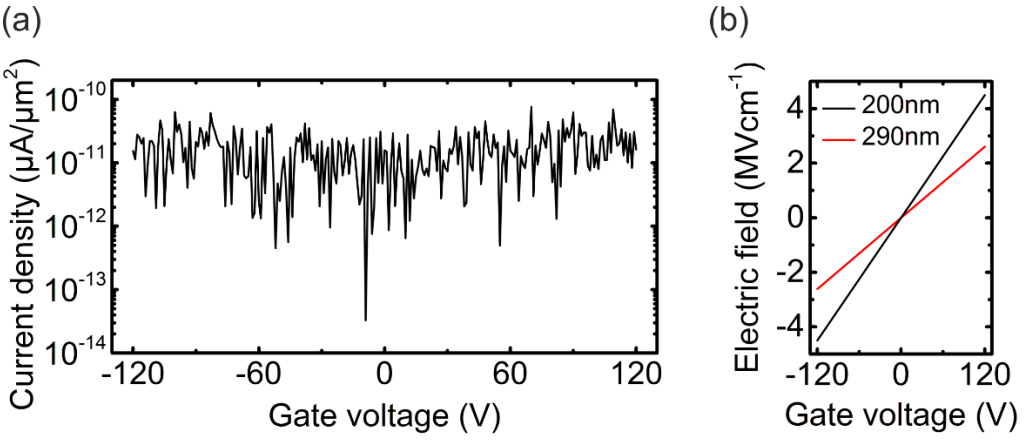

SI Figure 4. (a) Typical transfer curve of a photocapacitor device with the current density plotted as a function of the applied top-gate voltage on a semi-logarithmic scale. (b) Simulated electric field at the MoS_2 for devices with 200 nm SiO_2 (black) and 290 nm SiO_2 (red) as a function of the top-gate voltage.

SI Figure 4(a) shows a typical transfer characteristic of an as-fabricated photocapacitor device on a semi-logarithmic scale. The device suffers no leakage currents between -120 V to 120 V and is therefore suited for our measurements that require high electric fields. In order to possess a measure on the magnitude of the applied electric field directly at the MoS_2 crystal, we simulated the effective applied electric field using finite-element simulations (Comsol). The calculated electric field for the 200 nm and 290 nm device is plotted as a function of the applied top-gate voltage in SI figure 4(b). For the maximum voltages applied in the optical experiments (± 100 V) we effective apply electric fields of - 3.75 $MVcm^{-1}$ $\leq F \leq$ 3.75 $MVcm^{-1}$ (- 2.175 $MVcm^{-1}$ $\leq F \leq$ 2.175 $MVcm^{-1}$) for 200 nm SiO_2 covered Si (290 nm covered SiO_2) at the MoS_2 micro-crystallites.

S4 Gate voltage dependent photoluminescence spectra of N = 1 and N = 5

To provide the reader with detailed PL spectra for N = 1 and N = 5 we added SI figure 5 that shows the A-exciton PL for trace 2 and their corresponding transition energies for N = 1 and N = 5. SI figure 5(a) shows the A-exciton transition energy for N = 1 as a function of the applied gate voltage with corresponding PL spectra shown in SI figure 5(b). The gate voltage was tuned from V_G = - 60 V to V_G = 60 V. The A-exciton emission stems solely from trion emission. SI figure 5(c) shows the A-exciton transition energy for N = 5. Corresponding gate voltage dependent spectra are shown in SI figure 5(d). The emission at V_G = - 100 V features a weak amount of residual neutral exciton emission which quickly vanishes when tuning to V_G = 100 V supporting the conclusion that the observed energy shift arises from X^- subject to the quantum confined Stark effect.

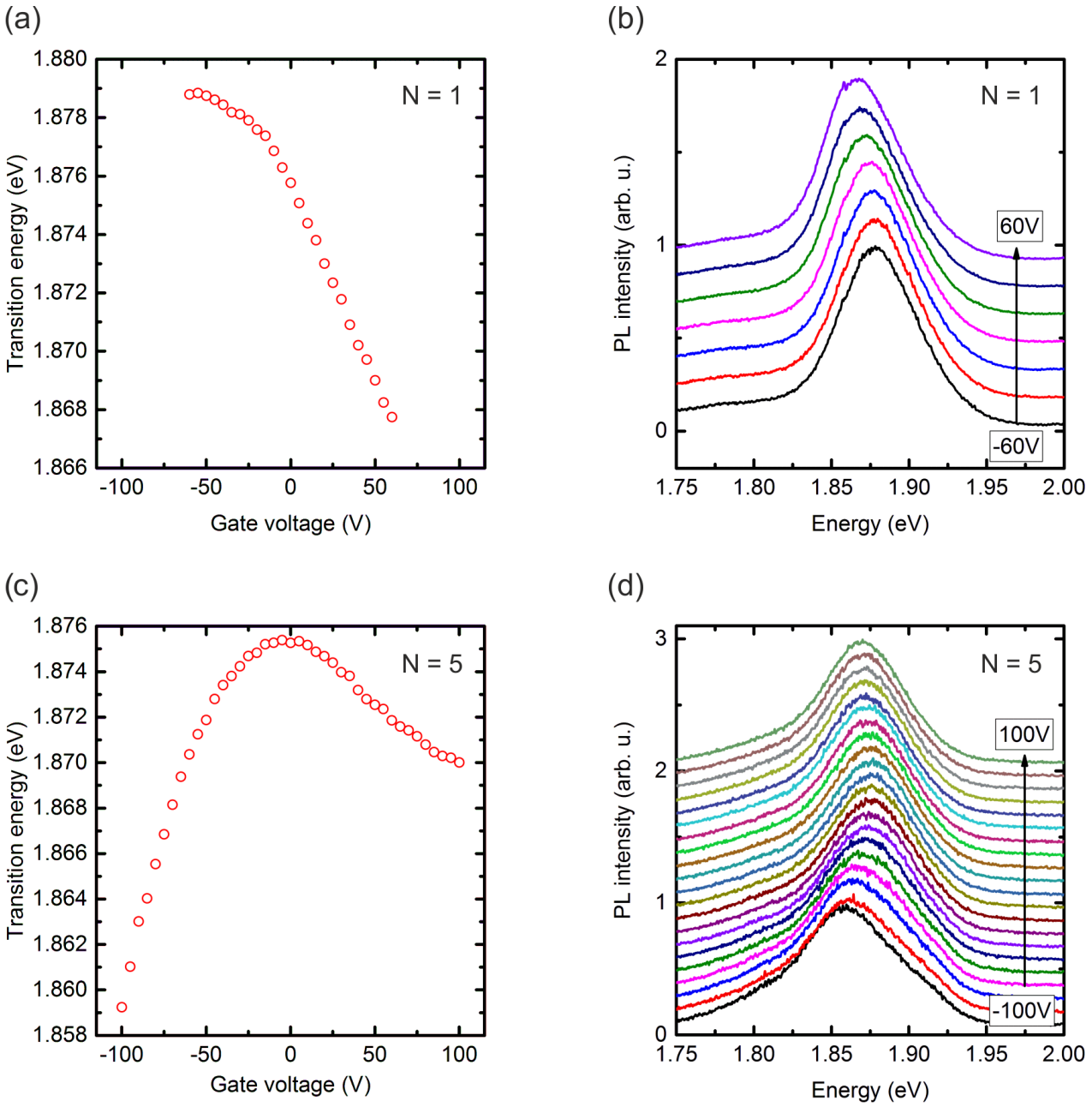

SI Figure 5. (a) Transition energy of the A-exciton for N = 1 as a function of the applied gate voltage. (b) The corresponding PL spectra when the applied voltage is tuned from V_G = - 60 V to V_G = 60 V. (c) Transition energy of the A-exciton for N = 5 as a function of the applied gate voltage. (d) The corresponding PL spectra when the applied voltage is tuned from V_G = - 100 V to V_G = 100 V.

S5 Electric field approximation

The effective applied electric field at position A/E in fig. 2(b) can be approximated using the following expression that describes the DC-Stark effect in a polarisable medium

$$\Delta E = -\beta \cdot F^2 - p \cdot F \quad (6)$$

Where, ΔE is the energy detuning (ΔE ~ (10 ± 1) meV) of the trion luminescence at A/E with respect to C/G, β the layer-independent A-exciton polarisability (β = (0.58 ± 0.25) × 10^{-8} DmV^{-1}) and p is the static dipole moment accounting for the possible polarisation of the exciton by the dielectric environment without an applied voltage. Solving SI eq. 6 for the electric field *F*, we obtain

$$F_{1/2} = \frac{-p \pm \sqrt{p^2 - 4 \cdot \beta \cdot (-\Delta E)}}{2 \cdot \beta}. \quad (7)$$

By assuming $p = 0$ (zero permanent excitonic dipole), this reduces to

$$F_{1/2} = \pm \sqrt{\frac{\Delta E}{\beta}}. \quad (8)$$

From this simple approach we can infer an effective applied electric field of $|F| = (2.88 \pm 0.64)$ $MVcm^{-1}$ at position A/E, orientated in a direction parallel to the out-of-plane direction, i.e. towards the Al_2O_3 layer.

S6 Second order perturbation model for quantum wells

The polarisability in quantum wells is described by the following expression obtained from second order perturbation theory[3]

$$\Delta E = \frac{\mu^* e^2 w^4}{\hbar^2} F^2 = \beta \cdot F^2 \quad (9)$$

with μ^* the reduced effective mass of electron and hole $\left(\frac{1}{\mu^*} = \frac{1}{m_e^*} + \frac{1}{m_h^*}\right)$, w the quantum well width and β the exciton polarisability. It is evident that $\beta(w) = \frac{\mu^* e^2 w^4}{\hbar^2}$ and the calculated polarisability as a function of the well width for typically reported values in the literature for the reduced effective mass ($\mu^* = (0.195 - 0.284)\, m_0$)[4-6] is plotted in SI figure 6(a) in addition to the experimentally obtained layer independent A-exciton polarisability $\langle \bar{\beta}_N \rangle$ = (0.58 ± 0.25) × 10^{-8} DmV^{-1} (dashed black line). The experimental polarisability and the calculated one is in good agreement with the theoretically expected well width which is on the order of less than 4.6 Å. This is about twice the covalent bond length of Mo and S (d_{Mo-S} = 2.4 Å) and less than the thickness of a single atomic layer of MoS_2 ($d_{(N=1)}$ = 6.5 Å).[7] Hence, the conclusion of an upper bound of the well width on the order of twice the covalent bond length of Mo and S and the conclusion of strongly confined excitons in each individual monolayer seems to be reasonable. We further used $\Delta E = \frac{\mu^* e^2 w^4}{\hbar^2} \cdot F^2$ to calculate the theoretically expected magnitude of the quantum confined Stark effect in order to compare it with the experimentally observed A-exciton detuning. Due to the error in the experimentally obtained polarisability (grey area in SI figure 6(a)), we chose to calculate the polarisability for the two cases which yield a minimum and a maximum value for the polarisability as depicted by the black and red circles in SI figure.6(a). The result is shown in SI figure 6(b) for w = 3.7 Å and μ^* = 0.284 m_0 (black curve) and for w = 5.1 Å and μ^* = 0.195 m_0 (red curve). In addition, the experimentally obtained A-exciton detuning for N = 5 (black circles) is shown. The magnitude of the experimentally obtained detuning is well within the expectation of this simple model which leads to a detuning on the order of 10 - 25 meV for electric fields of F = ± 3.75 MV/cm. SI figure 6(c) and SI figure 6(d) show the complete data set of the calculated A-exciton detuning as a function of the well width and applied electric field for μ^* = 0.284 m_0 and μ^* = 0.195 m_0 with the corresponding cuts (white dashed lines) that are shown in SI figure 6(b).

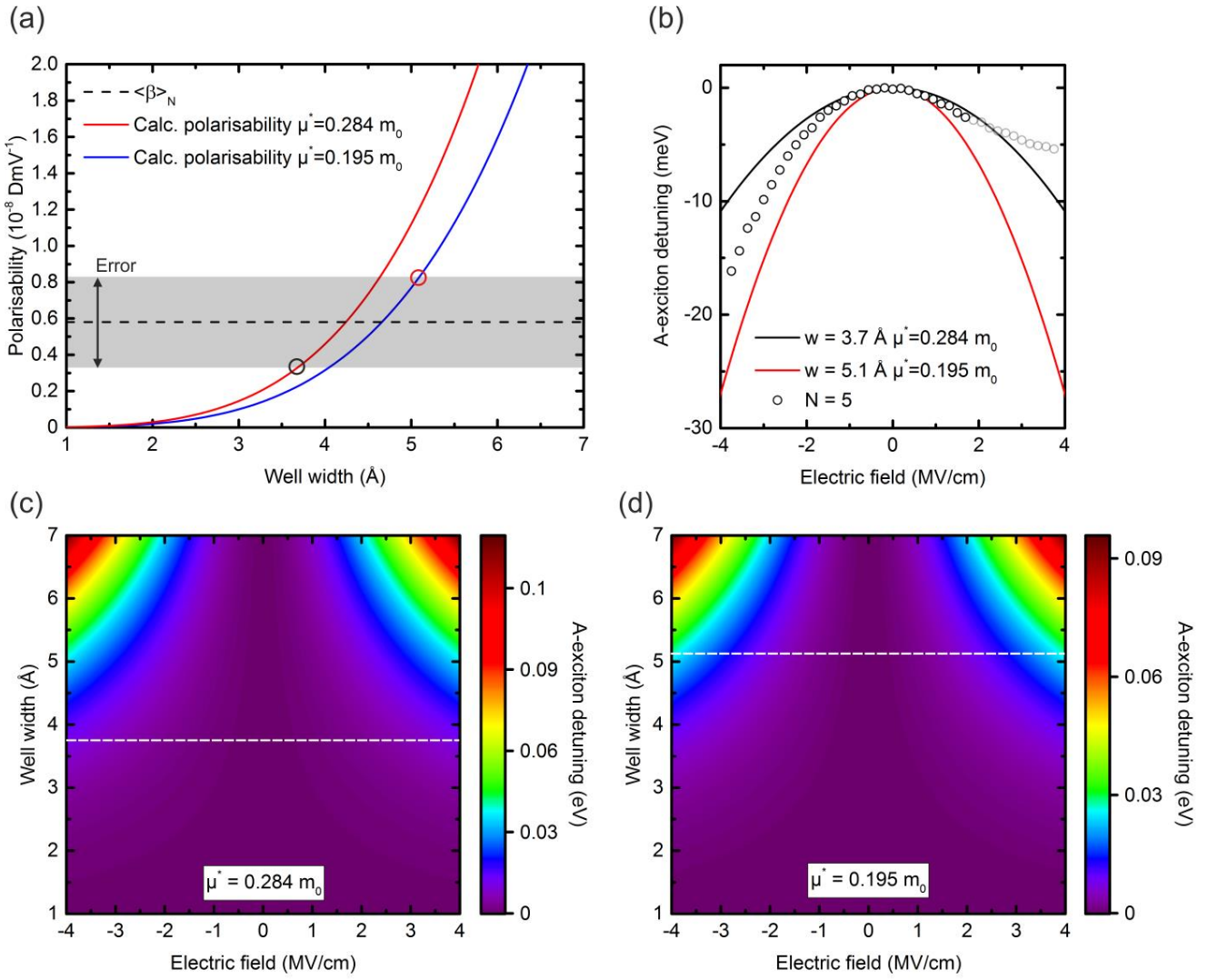

SI Figure 6. (a) Calculated polarisability from perturbation theory as a function of the well width for a reduced effective mass of $\mu^* = 0.284\ m_0$ (red curve) and $\mu^* = 0.195\ m_0$ (blue curve). The experimentally obtained polarisability is plotted with a dashed line with the error depicted as grey area. (b) Calculated A-exciton detuning for w = 3.7 Å and $\mu^* = 0.284\ m_0$ (black curve) and for w = 5.1 Å and $\mu^* = 0.195\ m_0$ (red curve) as marked with circles in (a) with experimental data for N = 5 (black circles). (c) Calculated detuning as a function of the well width and the applied electric field for $\mu^* = 0.284\ m_0$. (d) Calculated detuning for $\mu^* = 0.195\ m_0$. The cuts (white dashed lines) are plotted in (b).

REFERENCES

(1) Li, H.; Zhang, Q.; Yap, C. C. R.; Tay, B. K.; Edwin, T. H. T.; Olivier, A.; Baillargeat, D. *Adv. Func. Mat.* **2012**, 22, 1385-1390.

(2) Peters, K.; Tittel, A.; Gayer, N.; Graf, A.; Paulava, V.; Wurstbauer, U.; Hansen, W. *Appl. Phys. Lett.* **2011**, 99, 191912.

(3) Miller, D. A. B.; Chemla, D. S., Damen, T. C.; Gossard, A. C.; Wiegmann, W.; Wood, T. H.; Burrus, C. A. *Phys. Rev. Lett.* **1984**, 53, 2173.

(4) Cheiwchanchamnangij, T.; Lambrecht, W. R. L. *Phys. Rev. B* **2012**, 85, 205302.

(5) Yun, W. S.; Han, S. W.; Hong, S. C.; Kim, I. G.; Lee, J. D. *Phys. Rev. B* **2012**, 85, 033305.

(6) Ramasubramaniam, A. *Phys. Rev. B* **2012**, 86, 115409.

(7) Mattheiss, L. F. *Phys. Rev. B* **1973**, 8 3719.